Red Supergiant Stars within the Local Group

Lee. R. Patrick

Doctor of Philosophy
The University of Edinburgh
March 2016

Chapter 1

Chemistry and Kinematics of NGC 2100

1.1 Opening Remarks

Part of this work is submitted for publication in Patrick et al. (2016).

1.2 Introduction

Young massive clusters (YMCs[1]) are important probes of the early evolution of star clusters and have increasingly been used as tracers of star formation in galaxies (e.g. Whitmore & Schweizer, 1995; Miller et al., 1997; Zepf et al., 1999). Known to contain large populations of massive stars, YMCs are also important tracers of massive star formation, which is heavily clustered (Lada & Lada, 2003; de Wit et al., 2005; Parker & Goodwin, 2007). In addition to being the birthplace of most of the massive stars in the Local Universe ($> 200 \, M_\odot$ stars in R136; Crowther et al., 2010), owing to the density of stars, YMCs are thought to be the birthplace of some of the rich stellar exotica (e.g. blue stragglers, X-ray binaries and radio pulsars) found in the old population of globular clusters (GCs; Portegies Zwart, McMillan & Gieles, 2010).

---

[1]A YMC is defined as having an age of $< 100 \, \mathrm{Myr}$ and a stellar mass of $> 10^4 \, M_\odot$ (Portegies Zwart, McMillan & Gieles, 2010).

Recently, the idea that GCs are simple stellar populations has been called into question based on chemical anomalies of light elements (C, N, O, Na and Al; e.g. Gratton, Carretta & Bragaglia, 2012). These anomalies are considered by most authors to be the signature of multiple stellar populations within GCs. Studying YMCs could therefore potentially help to constrain some of the proposed models for creating multiple stellar populations within GCs (e.g. Cabrera-Ziri et al., 2014).

Investigating the link between YMCs and older clusters is an important, uncertain, factor in the evolution of young clusters. As most stellar systems are thought to dissolve shortly after formation (Lada & Lada, 2003), determining how long bound systems can remain so is an important question to answer. Studying the dynamical properties of YMCs is, therefore, an important tool to evaluate the likelihood that young clusters will survive. In addition, the study of YMCs in different environments can help bridge the gap between the understanding of star formation in the Solar neighbourhood and that in the high-redshift Universe.

Gazak et al. (2013) demonstrated that, after the appearance of the first RSGs within a YMC, the overall near-IR flux from the cluster is dominated by the RSGs ($F_{J,RSG}/F_J > 0.90$). Using this result, these authors showed that the spectrum from an unresolved star cluster can be used to estimate the average properties of the RSG population of the cluster using exactly the same analysis method as for single stars. Lardo et al. (2015) demonstrated this with KMOS spectroscopy of three unresolved YMCs in NGC 4038 in the Antennae ($d = 20\,\mathrm{Mpc}$), at Solar-like metallicity, finding good agreement with previous studies. With a multi-object spectrograph operating on the European Extremely Large Telescope, this technique could be used to measure metallicities of individual RSGs at distances of $> 10\,\mathrm{Mpc}$ and from YMCs out to potentially $> 100\,\mathrm{Mpc}$ (Evans et al., 2011).

NGC 2100 is a YMC in the Large Magellanic Cloud (LMC), located near the large star-forming 30 Doradus region. With an age of $\sim 20\,\mathrm{Myr}$ (Elson, 1991; Niederhofer et al., 2015), and a photometric mass of $4.6 \times 10^4 M_\odot$ (McLaughlin & van der Marel, 2005, assuming King (1966) profiles), NGC 2100 falls within the mass and age range where the near-IR cluster light is dominated by RSGs (Gazak et al., 2013). This is supported by the large number of RSGs identified within this cluster (see Figure 1.1).

NGC 2100 is not a cluster in isolation. It is located in one of the most actively star-forming regions within the Local Group of galaxies. At $\sim 20\,\mathrm{Myr}$ old, the most

massive members of this star cluster will have already exploded as supernovae. This should have had a profound effect on the surrounding gas and dust, and has potentially shaped the surrounding LMC 2 supershell (see Points et al., 1999).

In this study I estimate stellar parameters from KMOS spectroscopy for 14 RSGs which appear to be associated with NGC 2100. Section 1.3 describes the observations and data reduction, and in Section 1.4 I detail our results, focusing on radial velocities of the target stars where I derive the line-of-sight velocity dispersion, the dynamical mass of NGC 2100 and stellar parameters. Our results are discussed in Section 1.5 and conclusions are presented in Section 1.6.

1.3   Observations and Data Reduction

These observations were obtained as part of the KMOS Guaranteed Time Observations (PI: Evans 095.B-0022) in March 2015. The observations consisted of $8 \times 10\,\mathrm{s}$ exposures (seeing conditions $\sim1\rlap{.}''0$) taken with the YJ grating with sky offset exposures (S) interleaved between the object exposures (O) in an O, S, O observing pattern. In addition, a standard set of KMOS calibration frames were obtained as well as observations of HD 51506 (B5) as the telluric standard star. Figure 1.1 shows the observed RSGs overlaid on a J-band VISTA image of the surrounding region (Cioni et al., 2011).

The standard KMOS/esorex routines (SPARK; Davies, R. I. et al., 2013a) were used to calibrate and reconstruct the data cubes. Telluric correction was performed using the 24-arm telluric-correction routine using the methodology described in detail by Patrick et al. (2015). Briefly, corrections are made to the standard telluric recipe to account for slight differences in wavelength calibration between the telluric and science spectra. This is implemented using an iterative cross-correlation approach. Additionally, differences in the strength of the telluric features are corrected by applying a simple scaling using the equation:

$$T_2 = (T_1 + c)/(1 + c) \tag{1.1}$$

where T_2 is the scaled telluric-standard spectrum, T_1 is the uncorrected telluric-standard spectrum and c is the scaling parameter which is varied from $c = -0.5$ to $c = 0.5$ in increments of 0.02. The best value of c is chosen based on the overall
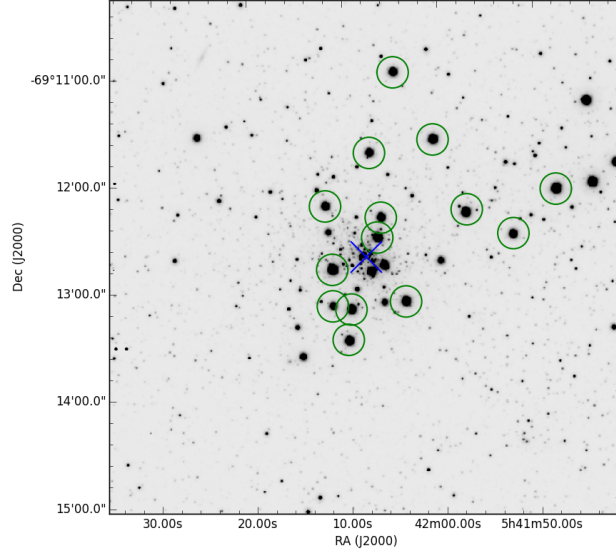
Figure 1.1 *Positions of the KMOS targets in NGC 2100 overlaid on a VISTA J-band image (Cioni et al., 2011). Green circles indicate KMOS targets. The adopted cluster centre has been marked by a blue cross.*

standard deviation of the spectrum, i.e. the c value producing the smallest σ is selected. Once these corrections are accounted for, the science spectra are divided by the appropriate telluric spectrum for that particular KMOS integral field unit (IFU).

1.4   Results

1.4.1   Radial velocities and velocity dispersion

Radial velocities are estimated using an iterative cross-correlation method. To ensure systematic shifts are removed, the observed spectra are first cross-correlated against a spectrum of the Earth's atmosphere, taken from the European Southern Observatory web pages[2], at a much higher spectral resolution than that of KMOS. This spectrum is then degraded to the resolution of the observations using a simple Gaussian filter. The cross-correlation is performed within the 1.140–1.155 μm region, as a strong set of reliable telluric features dominates this region, with minimal contamination from stellar features. The shift arising from this comparison is typically 0–10 km s^{-1} and is then applied to

4

Table 1.1 *Observed properties of VLT-KMOS targets in NGC 2100.*

ID	S/N	J^a	H^a	$K_s{}^a$	RV (km s^{-1})	Probabilities[c] P1	P2	Notes[b]
J054147.86−691205.9	320	9.525	8.603	8.200	250.3 ± 4.7	92	8	D15
J054152.51−691230.8	200	10.413	9.526	9.155	249.3 ± 2.6	93	7	D16
J054157.44−691218.1	200	9.811	9.036	8.738	245.6 ± 3.5	90	10	C2
J054200.74−691137.0	260	9.900	9.017	8.683	248.8 ± 2.7	92	8	C8
J054203.90−691307.4	250	9.839	8.996	8.740	251.1 ± 2.8	77	23	B4
J054204.78−691058.8	210	10.319	9.427	9.159	256.1 ± 4.0	92	8	. . .
J054206.36−691220.2	200	10.371	9.480	9.159	255.7 ± 4.9	84	16	B17
J054206.77−691231.1	250	9.977	9.150	8.807	250.6 ± 3.4	93	7	A127
J054207.45−691143.8	200	10.482	9.610	9.351	252.5 ± 3.0	78	22	C12
J054209.66−691311.2	240	9.976	9.136	8.841	254.3 ± 4.1	72	28	B47
J054209.98−691328.8	250	10.021	9.150	8.823	250.2 ± 3.0	34	66	C32
J054211.56−691248.7	300	9.557	8.617	8.264	255.5 ± 4.3	93	7	B40
J054211.61−691309.2	150	10.943	10.090	9.788	256.6 ± 6.1	74	26	B46
J054212.20−691213.3	200	10.440	9.622	9.335	260.0 ± 4.8	90	10	B22

[a] Photometric data from 2MASS, with typical errors on J, H, and K_s of 0.024, 0.026 and 0.022 mag respectively.
[b] Cross-identifications in final column from Robertson (1974).
[c] Probabilities $P1 = P(x|\{\mu,\sigma\}_{NGC\,2100}, \{\mu,\sigma\}_{LMC-field})$,
$P2 = P(x|\{\mu,\sigma\}_{LMC-field}, \{\mu,\sigma\}_{NGC\,2100})$

the science spectra so that they are on a consistent wavelength solution.

Stellar radial velocities are estimated following a similar approach to the methods used by Lapenna et al. (2015) and Patrick et al. (2015). An initial radial-velocity estimate is found for each star from cross-correlation of the KMOS spectra with an appropriate model spectrum in the 1.16–1.22 μm region (selected owing to the dominance of atomic features in RSG spectra at these wavelengths). The initial estimated is improved upon via an independent cross-correlation of the observed and model spectra for seven strong absorption lines in this region.

The quoted radial velocity for each star is the mean of these estimates, where the quoted uncertainty is the standard error of the mean (i.e. $\sigma/\sqrt{n_{\text{lines}}}$). Obvious outliers (with δRVs of tens of km s^{-1}) were excluded in calculating the mean estimates; such outliers arise occasionally from spurious peaks in the cross-correlation functions from noise/systematics in the spectra.

In order to sample from the posterior probability distribution for the intrinsic velocity dispersion and mean cluster velocity (given the observed radial velocity estimates and their uncertainties), emcee (Foreman-Mackey et al., 2013), an implementation of the affine-invariant ensemble sampler for Markov chain Monte Carlo (MCMC) of Goodman & Weare (2010), is used. likelihood function is

---

given by

$$p(D|\{\sigma_{1D}, v_0\}) = \prod_i \frac{1}{\sqrt{2\pi(\sigma_{1D}^2 + \sigma_{v,i}^2)}} \exp\left(\frac{-(v_i - v_0)^2}{2(\sigma_{1D}^2 + \sigma_{v,i}^2)}\right), \qquad (1.2)$$

where σ_{1D} is the intrinsic velocity dispersion of the cluster, v_0 is the mean cluster velocity, and the data consists of our set of radial velocity measurements v_i and their uncertainties $\sigma_{v,i}$. Therefore assume that the intrinsic cluster dispersion is Gaussian with no variations in the dispersion across the sample. The systemic radial velocity (v_0) of the sample is estimated to be $251.6 \pm 1.1\,\mathrm{km\,s^{-1}}$.

Figure 1.2 shows our stellar radial velocity estimates as a function of distance from the centre of the cluster, compared with the average radial velocity of ~ 200 massive stars within the LMC from Evans et al. (2015, green dashed line). To quantify the likelihood that the measured velocities are consistent with the NGC 2100 mean cluster velocity the probability that each measured velocity is drawn from a two-component mixture of Gaussian distributions with $P(x|\{\mu, \sigma\}_{NGC\,2100}) + P(x|\{\mu, \sigma\}_{LMC-field}) = 1$ is calculated, where the *LMC-field* distribution is defined by Evans et al. (2015). This allows us to calculate the ratio of the probabilities using the equation,

$$P(x|\{\mu, \sigma\}_X, \{\mu, \sigma\}_Y) = \frac{P(x|\{\mu, \sigma\}_X)}{P(x|\{\mu, \sigma\}_X) + P(x|\{\mu, \sigma\}_Y)}, \qquad (1.3)$$

where $P(x|\{\mu, \sigma\}_X)$ and $P(x|\{\mu, \sigma\}_Y)$ are the Gaussian distributions centred on the NGC 2100 systemic velocity or the LMC-field population as defined by Evans et al. (2015).

From this analysis one target (J054212.20−691.3) has a measured velocity with greater probability of being drawn from the underlying distribution of massive stars rather than the distribution centred on the NGC 2100 systemic velocity. Excluding this target from the sample does not alter the estimation of v_0 or σ_{1D} significantly, therefore this target is included for further analysis.

I conclude that all targets have a velocity consistent with membership to the LMC (as opposed to Galactic objects) and that none display compelling evidence for being excluded from membership of NGC 2100.

The estimated v_0 is in reasonable agreement with previous measurements for
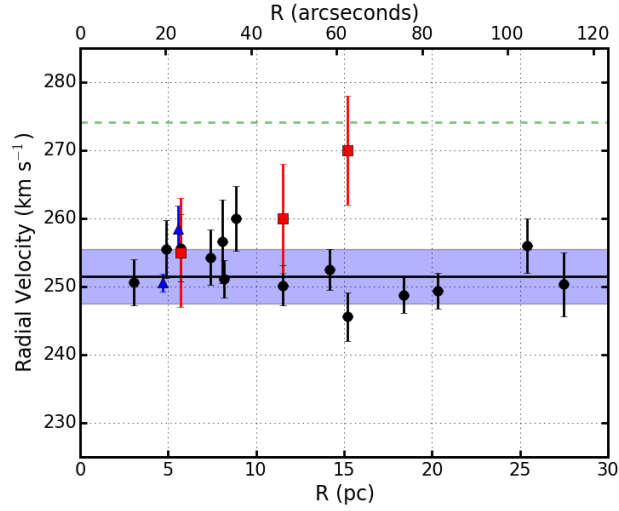
Figure 1.2 *Radial velocities of KMOS targets (black points) shown as a function of distance from the cluster centre. The green dashed line shows the LMC systemic velocity of ~200 massive stars from (274.1 ± 16.4 km s^{-1}; Evans et al., 2015). The solid black line shows the mean cluster velocity ($v_0 = 251.6 \pm 1.1$ km s^{-1}) and the shaded blue region shows $v_0 \pm \sigma_{1D}$. The blue triangles show estimates for two OB-type stars in NGC 2100 (Evans et al., 2015) and the red squares show previous estimates for three of our targets (Jasniewicz & Thevenin, 1994). The distance modulus used to produce this figure is 18.5 (Pietrzyński et al., 2013; de Grijs, Wicker & Bono, 2014).*

two OB-type stars in the cluster (Evans et al., 2015) as well as the results from four RSGs in NGC 2100 (Jasniewicz & Thevenin, 1994, henceforth JT94; three of which were observed in the current study). Table 1.2 contains the details of previous radial velocity measurements within NGC 2100. I conclude that there exists no significant difference between our measurements and previous estimates within NGC 2100. This is an additional confirmation that absolute radial velocities can be precisely measured with KMOS spectra.

As shown in Figure 1.3, the line-of-sight velocity dispersion (σ_{1D}) of NGC 2100 is

Table 1.2 *Literature stellar radial-velocity measurements within NGC 2100.*

ID		RV (km s^{-1})		Reference	Notes
Lit.	current study	Lit.	current study		
AAΩ 30 Dor 407	—	258.5 ± 3.4	. . .	Evans et al. (2015)	O9.5 II
AAΩ 30 Dor 408	—	250.6 ± 1.3	. . .	Evans et al. (2015)	B3 Ia
R74 B17	J054206.36-691220.2	255 ± 8	255.7 ± 4.9	Jasniewicz & Thevenin (1994)	
R74 C2	J054157.44-691218.1	270 ± 8	245.6 ± 3.5	Jasniewicz & Thevenin (1994)	
R74 C32	J054209.98-691328.8	260 ± 8	250.2 ± 3.0	Jasniewicz & Thevenin (1994)	
R74 C34	—	265 ± 8	. . .	Jasniewicz & Thevenin (1994)	

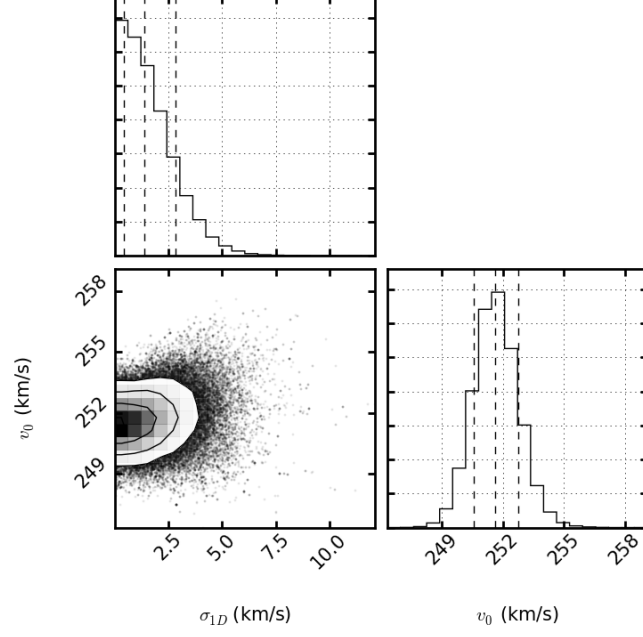ID and RV columns: the first value is from the literature and the second is from the current study.

Figure 1.3 *One- and two-dimensional projections of the posterior probability distributions of the line-of-sight velocity dispersion (σ_{1D}) and systemic velocity (v_0) for NGC 2100 assuming the dispersion is Gaussian and constant over the range measured using. Using this method the velocity of NGC 2100 is $251.6 \pm 1.1\,km\,s^{-1}$. This figure also demonstrates that the velocity dispersion for the sample is unresolved and therefore an upper limit on $\sigma_{1D} < 3.9\,km\,s^{-1}$ at the 95% confidence level is placed.*

unresolved given the current data. Therefore an upper limit on $\sigma_{1D} < 3.9\,\mathrm{km\,s^{-1}}$ at the 95% confidence level is adopted. Figure 1.4 demonstrates that there is no evidence for spatial variations in the measured σ_{1D} and it is noted that in each radial bin (which contain 5, 4 and 5 stars respectively), the measured dispersion is unresolved.

1.4.2 Dynamical mass

Using σ_{1D} as an upper limit on the velocity distribution, one can calculate an upper limit on dynamical mass of the cluster using the virial equation:

$$M_{dyn} = \frac{\eta \sigma_{1D}^2 r_{\mathrm{eff}}}{G} \tag{1.4}$$

where M_{dyn} is the dynamical mass and $\eta = 6r_{vir}/r_{\mathrm{eff}} = 9.75$ – providing the
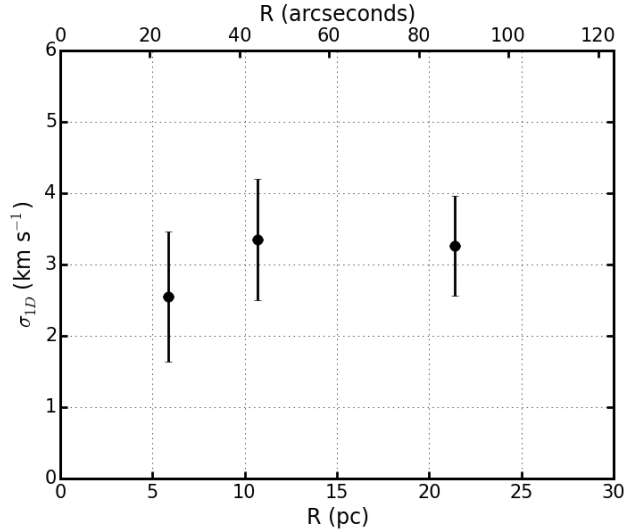
Figure 1.4 *Upper limits to the line-of-sight velocity dispersion for the NGC 2100 RSGs in three radial bins as a function of the distance from the centre of NGC 2100. This figure demonstrates that there is no evidence for spatial variations in σ_{1D}. However, it is noted that in each radial bin the underlying dispersion is unresolved (see Figure 1.3).*

density profile of the cluster is sufficiently steep (Portegies Zwart, McMillan & Gieles, 2010) – where $r_{\mathrm{eff}} = 4.41\,\mathrm{pc}$ for NGC 2100 (McLaughlin & van der Marel, 2005). However, NGC 2100 has a relatively shallow density profile ($\gamma = 2.44\pm0.14$; Mackey & Gilmore, 2003) which means $\eta < 9.75$. Using $\sigma_{1D} = 3.9\,\mathrm{km\,s^{-1}}$ and equation 1.4, an upper limit on the dynamical mass of NGC 2100 is $M_{dyn} = 15.2 \times 10^4 M_{\odot}$. Comparing this to the photometric mass $M_{phot} = (2.3 \pm 1.0) \times 10^4 M_{\odot}$ (McLaughlin & van der Marel, 2005), the upper limit on the dynamical mass is larger.

As discussed by Gieles, Sana & Portegies Zwart (2010), binary motions can increase the measured velocity dispersion profile (e.g. see Hénault-Brunet et al., 2012). However, as Gieles, Sana & Portegies Zwart (2010) note, the mean lifetime for RSGs in binary systems is significantly decreased and, where mass transfer occurs, their number decrease dramatically (Eldridge, Izzard & Tout, 2008). Therefore it is expected that the number of RSGs in close binaries is small (Feast, 1979; Davies et al., 2009). The fraction of RSGs in longer-period systems is less certain, but these would contribute substantially less to the line-of-sight velocity distribution.

These arguments suggest that our estimate for the velocity dispersion in NGC 2100 is not significantly increased by binary motions as our target stars

are expected to be (predominantly) single objects. As the true dispersion of the cluster appears to be unresolved (Figure 1.3), it is concluded therefore that the upper limit of the dynamical mass is consistent with the published photometric mass.

Evidence in the literature suggests that J054211.61−691309.2 is an eclipsing binary system VV Cep (Feast, 1979). However, the radial velocity of this star ($256.6 \pm 6.1 \, \mathrm{km \, s^{-1}}$) does not appear to be increased as a result of binary motions, with respect to the sample studied here.

1.4.3 Stellar parameters

Stellar parameters are estimated for each target using the J-band analysis technique described initially by Davies, Kudritzki & Figer (2010) and tested rigorously by Gazak et al. (2014b) and Davies et al. (2015). These studies show that by using a narrow spectral window within the J-band one can accurately derive overall metallicities ($[\mathrm{Z}] = \log(\mathrm{Z}/\mathrm{Z}_\odot)$) to better than $\pm 0.15 \, \mathrm{dex}$ at the resolution of KMOS observations with S/N $\geq$ 100. Patrick et al. (2015) built on this by demonstrating the feasibility of this technique using KMOS spectra.

The analysis uses synthetic RSG spectra, extracted from MARCS model atmospheres (Gustafsson et al., 2008), computed with corrections for non-local thermodynamic equilibrium for lines from titanium, iron, silicon and magnesium (Bergemann et al., 2012, 2013, 2015). The parameter ranges for the grid of synthetic RSG spectra are listed in Table 1.3. The synthetic spectra are compared with observations using the χ-squared statistic and the synthetic spectra are degraded to the resolution and sampling of the observations. The diagnostic spectral features used to estimate stellar parameters have equal weighting in the analysis.

Estimated stellar parameters are listed in Table 1.4. Figure 1.5 shows the observed KMOS spectra (black) compared to their best-fitting models (red). The average metallicity for the 14 RSGs is $[\mathrm{Z}] = -0.38 \pm 0.20 \, \mathrm{dex}$ where the large scatter is a result of the contribution from (J054211.61−691309.2). Excluding this apparent outlier yields an average metallicity of $[\mathrm{Z}] = -0.43 \pm 0.10 \, \mathrm{dex}$, which reduces the scatter and does not alter the result significantly. The model fit parameters of J054211.61−691309.2 suggest a considerably ($\times 1.7$) super-solar metallicity. This appears unlikely given its apparent membership the LMC,

Table 1.3 *Model grid used for the spectroscopic analysis.*

Model Parameter	Min.	Max.	Step size
T_{eff} (K)	3400	4400	100
[Z] (dex)	-1.0	1.0	0.1
$\log g$ (cgs)	-1.00	1.00	0.25
ξ (km s^{-1})	1.0	5.0	0.2

and it is notable that the estimates for the surface gravity and microturbulence parameters are also outliers compared to the rest of the sample. In addition, as noted above, this star was flagged as a potential eclipsing binary by (Feast, 1979), therefore this target is excluded from the sample in further analysis.

The average metallicity in NGC 2100 estimated here is in good agreement with estimates of the cluster metallicity using isochrone fitting to the optical colour-magnitude diagram (-0.34 dex; Niederhofer et al., 2015). The only other estimate of stellar metallicity within this cluster is from JT94 who estimated metallicities using optical spectroscopy of four RSGs. These authors found an average metallicity for NGC 2100 of [Fe/H] $= -0.32 \pm 0.03$ dex, which is in reasonable agreement with our estimate. There are three targets in common with our study: B17, C2 and C32 (using the Robertson, 1974, nomenclature). Given the differences in the analyses (i.e. optical cf. infrared, and the different models used) the estimated parameters are in reasonable agreement for all three stars (aside from the spectroscopic gravities quoted by JT94, but with reasonable agreement with their photometric gravity estimates).

Using the same analysis technique as in this study, Davies et al. (2015) estimate metallicities for nine RSGs within the LMC, finding an average value of [Z] $= -0.37 \pm 0.14$ dex, which our estimate agrees well with. In Figure 1.6, the effective temperatures and metallicities from NGC 2100 are compared with those estimated for RSGs elsewhere in the LMC. Good agreement is found in the distribution of temperatures from the two studies, with the average agreeing well. The range in [Z] from the LMC population is slightly larger than that of the NGC 2100 RSGs, which is expected when comparing a star cluster with an entire galaxy; however, the averages for the two studies agree very well.
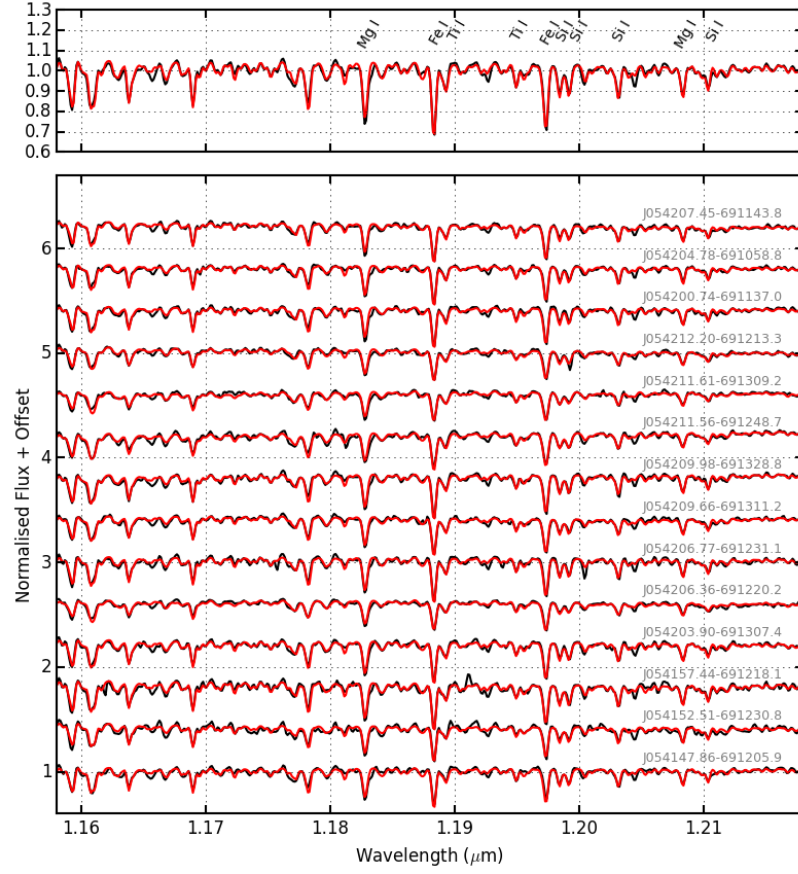
Figure 1.5 *KMOS spectra of RSGs in NGC 2100 and their associated best-fit models (black and red lines, respectively). The upper panel shows the simulated integrated-light cluster spectrum; the lower panel shows spectra for the individual RSGs. The lines used for the analysis, from left-to-right by species, are Fe I λλ1.188285, 1.197305; Mg I λλ1.182819, 1.208335; Si I λλ1.198419, 1.199157, 1.203151, 1.210353; Ti I λλ1.189289, 1.194954.*
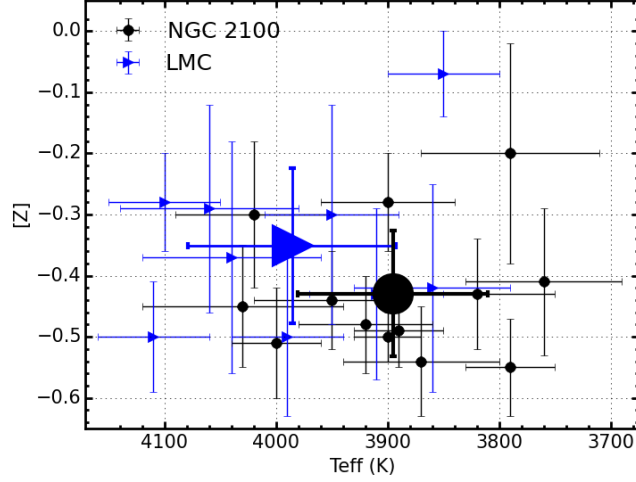
Figure 1.6 *Estimated metallicities for NGC 2100 RSGs in this study shown against effective temperature (black points). For comparison the distribution of LMC RSGs from Davies et al. (2015, blue triangles) is shown with good agreement between the means of the two samples.*

Table 1.4 *Physical parameters determined for the KMOS targets in NGC 2100.*

Target	IFU	ξ (km s^{-1})	[Z]	$\log g$	T_{eff} (K)	Notes[a]
J054147.86−691205.9	7	3.6 ± 0.2	-0.45 ± 0.10	0.10 ± 0.16	4030 ± 90	D15
J054152.51−691230.8	9	3.6 ± 0.2	-0.51 ± 0.09	0.43 ± 0.18	4000 ± 40	D16
J054157.44−691218.1	6	4.9 ± 0.1	-0.44 ± 0.08	0.15 ± 0.20	3950 ± 70	C2
J054200.74−691137.0	4	4.2 ± 0.2	-0.55 ± 0.08	0.23 ± 0.10	3790 ± 40	C8
J054203.90−691307.4	12	4.5 ± 0.2	-0.49 ± 0.06	0.23 ± 0.09	3890 ± 40	B4
J054204.78−691058.8	3	4.2 ± 0.2	-0.54 ± 0.09	0.46 ± 0.15	3870 ± 70	. . .
J054206.36−691220.2	24	2.8 ± 0.4	-0.20 ± 0.18	0.42 ± 0.18	3790 ± 80	B17
J054206.77−691231.1	10	4.9 ± 0.2	-0.50 ± 0.04	0.25 ± 0.09	3900 ± 30	A127
J054207.45−691143.8	2	4.0 ± 0.2	-0.43 ± 0.09	0.45 ± 0.17	3820 ± 70	C12
J054209.66−691311.2	14	3.8 ± 0.2	-0.41 ± 0.12	0.06 ± 0.20	3760 ± 70	B47
J054209.98−691328.8	11	4.8 ± 0.1	-0.48 ± 0.08	0.17 ± 0.22	3920 ± 60	C32
J054211.56−691248.7	20	3.8 ± 0.2	-0.28 ± 0.08	0.01 ± 0.16	3900 ± 60	B40
J054211.61−691309.2	18	2.2 ± 0.4	0.23 ± 0.23	0.65 ± 0.19	3800 ± 100	B46
J054212.20−691213.3	22	3.3 ± 0.2	-0.30 ± 0.12	0.33 ± 0.31	4020 ± 70	B22
NGC 2100 average[b]		4.0 ± 0.6	-0.43 ± 0.10	0.25 ± 0.15	3900 ± 85	
Integrated-light spectrum[c]		4.6 ± 0.3	-0.42 ± 0.14	0.37 ± 0.22	3860 ± 85	

[a] ID in final column from Robertson (1974).
[b] Averages computed excluding J054211.61−691309.2. See text for details.
[c] Simulated integrated light cluster spectrum parameters estimated excluding J054211.61−691309.2.

1.5 Discussion

1.5.1 Stellar parameters

Luminosities have been estimated for our sample from K-band photometry (see Table 1.1) using the bolometric correction from Davies, B. et al. (2013b) with a small contribution from interstellar extinction using E(B−V) = 0.17 (Niederhofer et al., 2015) assuming $R_V = 3.5$ (Doran et al., 2013) and $A_K/A_V = 0.112$ (Rieke & Lebofsky, 1985). The H–R diagram for the cluster is presented in Figure 1.7. Overlaid on this H–R diagram are SYCLIST stellar isochrones for SMC-like (solid lines; Georgy et al., 2013) and Solar-like (dashed lines; Ekström et al., 2012) models, where stellar rotation is 40% of break-up velocity. Even though the temperatures covered by the SMC-like models do not represent the distribution of temperatures observed in this study, they remain useful to constrain the age of NGC 2100. The Solar-like models (dashed) demonstrate that, when compared with the SMC-like models, increasing the metallicity of the sample (a) decreases the average temperature of the RSGs (something which is not observed by Patrick et al., 2015), (b) induces so called 'blue loop' behaviour for the youngest models and (c) decreases the luminosity for the youngest models.

In addition, results for 11 RSGs from the Galactic star cluster Perseus OB-1 (PerOB1; Gazak et al., 2014a) are overlaid in Figure 1.7 (blue stars) for which stellar parameters were estimated using the same analysis technique as in this study. PerOB1 is a cluster with a similar mass and age ($2 \times 10^4 \, M_\odot$ and 14 Myr respectively; Currie et al., 2010) as NGC 2100, and a comparison between the stellar components of these two clusters using a consistent analysis technique is useful to highlight differences in stellar evolution within clusters at this range of metallicities.

From Figure 1.7, generally, the estimated temperatures are in good agreement between the two clusters. The median luminosity for the PerOB1 targets ($10^{4.93\pm0.15} \, L_\odot$) is slightly above that of NGC 2100 ($10^{4.77\pm0.15} \, L_\odot$) which could represent the slight difference in the ages of the two clusters. As PerOB1 is younger, the average mass for a RSG in the cluster will be larger than the average in NGC 2100. Therefore, I would expect to see higher luminosity RSGs in PerOB1. However, the difference between the two samples is barely significant and is consistent with a constant luminosity. The average effective temperatures
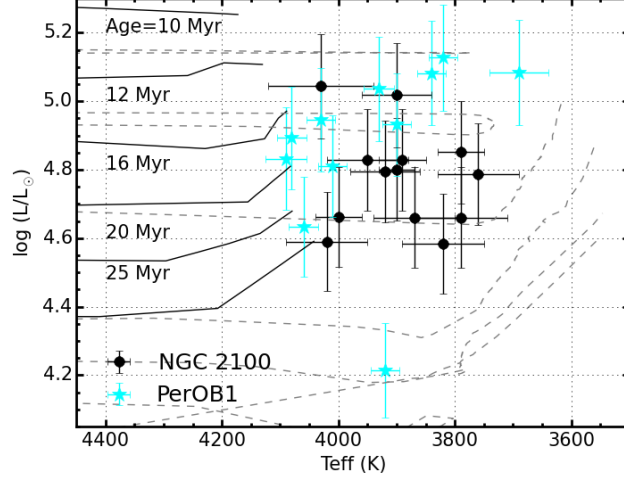
Figure 1.7 *H–R diagram for 14 RSGs in NGC 2100 (black points). Isochrones for solar (dashed grey lines; Ekström et al., 2012) and SMC-like (solid black lines; Georgy et al., 2013) metal abundances, in which stellar rotation is 40% of the break-up velocity, are shown for ages of 10-32 Myr. For comparison, 11 RSGs from the Galactic YMC Perseus OB-1 are overlaid with cyan stars (Gazak et al., 2014b). The best-fit isochrone to the observed data has an age of 20 ± 5 Myr for both SMC- and solar-like metallicities.*

for the two data sets (NGC 2100: 3910 ± 15 K, PerOB1: 3940 ± 10 K) are in reasonable agreement, where the spread in temperatures is slightly larger for PerOB1 ($\sigma_{\mathrm{PerOB1}} = 120$ K, $\sigma_{\mathrm{NGC\,2100}} = 90$), particularly so for the highest luminosity targets within the PerOB1 sample. Overall, by comparing these two star clusters with a similar mass, age and stellar population, I conclude that there exists no significant difference in appearance on the H–R diagram of RSGs within star clusters of different metallicities.

1.5.2 Simulated cluster spectrum analysis

Using the individual stars in NGC 2100 to simulate the analysis of a YMC in the more distant Universe, assuming that RSGs dominate the near-IR flux from such a cluster (Gazak et al., 2013). Gazak et al. (2014b) use this assumption to create a simulated integrated-light cluster spectrum for PerOB1 and show that, by analysing the combined spectrum from their 11 RSGs, the resulting parameters are consistent with the average parameters estimated using the individual stars. NGC 2100 has a similar mass and age to PerOB1 and Gazak et al. (2014b) study a similar number of RSGs to this study, therefore, a direct comparison between

the two clusters is useful to investigate potential metallicity dependencies.

To create a simulated integrated-light cluster spectrum the individual RSG spectra are summed and weighted by their J-band luminosities. The resulting spectrum is then degraded to the lowest resolution spectrum of the sample using a simple Gaussian filter. The top panel of Figure 1.5 shows the resulting integrated-light cluster spectrum. This spectrum is then analysed in the same way described in Section 1.4.3 for a single RSG. The results of this analysis are what one would expect from KMOS observations of more distant YMCs where individual stars cannot be resolved. The estimated parameters for this spectrum are, a metallicity of -0.35 ± 0.07 dex, an effective temperature of 3960 ± 70 K, a surface gravity of 0.64 ± 0.19 dex and a microturbulent velocity of 4.6 ± 0.2 km s^{-1} which agree well with the averages of the individual RSG parameters.

1.5.3 Velocity dispersion and dynamical mass

This study represents the first estimate of an upper limit to the line-of-sight velocity dispersion profile for NGC 2100. Comparing this estimate with that of other YMCs in the Local Universe is useful to ascertain if this cluster shares similar properties with other YMCs. The properties NGC 2100 are well matched by other clusters with similar masses and ages, particularly so with RSGC01, a Galactic YMC (Davies et al., 2007).

Owing to the non-negligible contribution from measurement errors, the σ_{1D} adopted here is an upper limit to the true dispersion within the cluster which is likely to be significantly smaller. Using the data available, σ 3.9 km s^{-1}to the 95% confidence level, however, the true dispersion of the cluster is unresolved.

By extension, the dynamical mass estimated here is therefore also an upper limit to the true mass of the cluster. There are several factors that could alter the value of the dynamical mass estimate. The likely value of the η parameter is discussed in Section 1.4.2 and any change in this value will act to decrease the estimated dynamical mass.

1.6   Conclusions

Using KMOS spectra of 14 RSGs in NGC 2100 for the first time the dynamical properties of this cluster have been estimated. Radial velocities have been estimated using KMOS, to a precision of $< 5\,\mathrm{km\,s^{-1}}$, demonstrating that this instrument can be used to study the dynamical properties of star clusters in external galaxies.

An upper limit to the average line-of-sight velocity dispersion of $\sigma_{1D} = 3.9\,\mathrm{km\,s^{-1}}$ has been estimated, at the 95% confidence level, and no evidence is found for spatial variations. Using the average velocity dispersion within NGC 2100 allows an upper limit on the dynamical mass to be calculated (assuming virial equilibrium) as $M_{dyn} = 15.2 \times 10^4 M_\odot$. This measurement is consistent with the literature measurement of the photometric mass (McLaughlin & van der Marel, 2005) as the true dispersion is unresolved.

In addition to estimating the dynamical properties of NGC 2100, stellar parameters have been estimated for 14 RSGs in NGC 2100 using the J-band analysis technique (Davies, Kudritzki & Figer, 2010). The average metallicity for RSGs in NGC 2100 is $[Z] = -0.43 \pm 0.10\,\mathrm{dex}$, which agrees well with previous studies within this cluster and with studies of the young stellar population of the LMC.

The H–R diagram of NGC 2100 is compared with that of PerOB1: a Galactic YMC with a similar age, mass and stellar population. Using stellar parameters estimated from RSGs using the same analysis technique as in this study, this study demonstrate that there exists no significant difference in the appearance of the H–R diagram of YMCs between Solar- and LMC-like metallicities.

By combining the individual RSG spectra within NGC 2100, I have simulated an integrated-light cluster spectrum and proceeded to analyse this spectrum using the same techniques for that of the individual RSGs, as RSGs dominate the cluster light in the J-band (Gazak et al., 2013). The results of this technique demonstrate the potential of this analysis for integrated light spectra of more distant YMCs in low-metallicity environments. I find good agreement using the integrated-light cluster spectrum with the average results of the individual RSGs.

Bibliography

Bergemann M., Kudritzki R.-P., Gazak Z., Davies B., Plez B., 2015, ApJ, 804, 113

Bergemann M., Kudritzki R.-P., Plez B., Davies B., Lind K., Gazak Z., 2012, ApJ, 751, 156

Bergemann M., Kudritzki R.-P., Würl M., Plez B., Davies B., Gazak Z., 2013, ApJ, 764, 115

Cabrera-Ziri I., Bastian N., Davies B., Magris G., Bruzual G., Schweizer F., 2014, MNRAS, 441, 2754

Cioni M.-R. L. et al., 2011, A&A, 527, A116

Crowther P. A., Schnurr O., Hirschi R., Yusof N., Parker R. J., Goodwin S. P., Kassim H. A., 2010, MNRAS, 408, 731

Currie T. et al., 2010, ApJS, 186, 191

Davies B., Figer D. F., Kudritzki R.-P., MacKenty J., Najarro F., Herrero A., 2007, ApJ, 671, 781

Davies B., Kudritzki R.-P., Figer D. F., 2010, MNRAS, 407, 1203

Davies B., Kudritzki R.-P., Gazak Z., Plez B., Bergemann M., Evans C., Patrick L., 2015, ApJ, 806, 21

Davies B., Origlia L., Kudritzki R.-P., Figer D. F., Rich R. M., Najarro F., Negueruela I., Clark J. S., 2009, ApJ, 696, 2014

Davies, B. et al., 2013b, ApJ, 767, 3

Davies, R. I. et al., 2013a, A&A, 558, A56

de Grijs R., Wicker J. E., Bono G., 2014, AJ, 147, 122

de Wit W. J., Testi L., Palla F., Zinnecker H., 2005, A&A, 437, 247

Doran E. I. et al., 2013, A&A, 558, A134

Ekström S. et al., 2012, A&A, 537, A146

Eldridge J. J., Izzard R. G., Tout C. A., 2008, MNRAS, 384, 1109

Elson R. A. W., 1991, ApJS, 76, 185

Evans C. J. et al., 2011, A&A, 527, A50

Evans C. J., van Loon J. T., Hainich R., Bailey M., 2015, A&A, 584, A5

Feast M. W., 1979, MNRAS, 186, 831

Foreman-Mackey D., Hogg D. W., Lang D., Goodman J., 2013, PASP, 125, 306

Gazak J. Z., Bastian N., Kudritzki R.-P., Adamo A., Davies B., Plez B., Urbaneja M. A., 2013, MNRAS, 430, L35

Gazak J. Z. et al., 2014a, ApJ, 787, 142

Gazak J. Z., Davies B., Kudritzki R., Bergemann M., Plez B., 2014b, ApJ, 788, 58

Georgy C. et al., 2013, A&A, 558, A103

Gieles M., Sana H., Portegies Zwart S. F., 2010, MNRAS, 402, 1750

Goodman J., Weare J., 2010, Comm. App. Math. Comp. Sci., 1, 65

Gratton R. G., Carretta E., Bragaglia A., 2012, A&A Rev., 20, 50

Gustafsson B., Edvardsson B., Eriksson K., J rgensen U. G., Nordlund Å., Plez B., 2008, A&A, 486, 951

Hénault-Brunet V. et al., 2012, A&A, 546, A73

Jasniewicz G., Thevenin F., 1994, A&A, 282, 717

King I. R., 1966, AJ, 71, 64

Lada C. J., Lada E. A., 2003, ARA&A, 41, 57

Lapenna E., Origlia L., Mucciarelli A., Lanzoni B., Ferraro F. R., Dalessandro E., Valenti E., Cirasuolo M., 2015, ApJ, 798, 23

Lardo C., Davies B., Kudritzki R.-P., Gazak J. Z., Evans C. J., Patrick L. R., Bergemann M., Plez B., 2015, ApJ, 812, 160

Mackey A. D., Gilmore G. F., 2003, MNRAS, 338, 85

McLaughlin D. E., van der Marel R. P., 2005, ApJS, 161, 304

Miller B. W., Whitmore B. C., Schweizer F., Fall S. M., 1997, AJ, 114, 2381

Niederhofer F., Hilker M., Bastian N., Silva-Villa E., 2015, A&A, 575, A62

Parker R. J., Goodwin S. P., 2007, MNRAS, 380, 1271

Patrick L. R., Evans C. J., Davies B., Kudritzki R., Hénault-Brunet V., Bastian N., Lapenna E., Bergemann M., 2016, ArXiv e-prints

Patrick L. R., Evans C. J., Davies B., Kudritzki R.-P., Gazak J. Z., Bergemann M., Plez B., Ferguson A. M. N., 2015, ApJ, 803, 14

Pietrzyński G. et al., 2013, Nature, 495, 76

Points S. D., Chu Y. H., Kim S., Smith R. C., Snowden S. L., Brandner W., Gruendl R. A., 1999, ApJ, 518, 298

Portegies Zwart S. F., McMillan S. L. W., Gieles M., 2010, ARA&A, 48, 431

Rieke G. H., Lebofsky M. J., 1985, ApJ, 288, 618

Robertson J. W., 1974, A&AS, 15, 261

Whitmore B. C., Schweizer F., 1995, AJ, 109, 960

Zepf S. E., Ashman K. M., English J., Freeman K. C., Sharples R. M., 1999, AJ, 118, 752